2015

Strengthening mechanisms in thermomechanically processed NbTi-microalloyed steel

Andrii Kostryzhev
University of Wollongong, andrii@uow.edu.au

Olexandra Marenych
University of Wollongong, marenych@uow.edu.au

Chris R. Killmore
BlueScope Steel Limited

Elena V. Pereloma
University of Wollongong, elenap@uow.edu.au

Publication Details

Kostryzhev, A. G., Marenych, O. O., Killmore, C. R. & Pereloma, E. V. (2015). Strengthening mechanisms in thermomechanically processed NbTi-microalloyed steel. Metallurgical and Materials Transactions A: Physical Metallurgy and Materials Science, 46 (8), 3470-3480.

Strengthening mechanisms in thermomechanically processed NbTi-microalloyed steel

Abstract
The effect of deformation temperature on microstructure and mechanical properties was investigated for thermomechanically processed NbTi-microalloyed steel with ferrite-pearlite microstructure. With a decrease in the finish deformation temperature at 1348 K to 1098 K (1075 °C to 825 °C) temperature range, the ambient temperature yield stress did not vary significantly, work hardening rate decreased, ultimate tensile strength decreased, and elongation to failure increased. These variations in mechanical properties were correlated to the variations in microstructural parameters (such as ferrite grain size, solid solution concentrations, precipitate number density and dislocation density). Calculations based on the measured microstructural parameters suggested the grain refinement, solid solution strengthening, precipitation strengthening, and work hardening contributed up to 32 pct, up to 48 pct, up to 25 pct, and less than 3 pct to the yield stress, respectively. With a decrease in the finish deformation temperature, both the grain size strengthening and solid solution strengthening increased, the precipitation strengthening decreased, and the work hardening contribution did not vary significantly.

Keywords
mechanisms, processed, strengthening, thermomechanically, steel, microalloyed, nbti

Disciplines
Engineering | Science and Technology Studies

Publication Details
Kostryzhev, A. G., Marenych, O. O., Killmore, C. R. & Pereloma, E. V. (2015). Strengthening mechanisms in thermomechanically processed NbTi-microalloyed steel. Metallurgical and Materials Transactions A: Physical Metallurgy and Materials Science, 46 (8), 3470-3480.

Strengthening Mechanisms in Thermomechanically Processed NbTi-Microalloyed Steel

ANDRII G. KOSTRYZHEV, OLEXANDRA O. MARENYCH, CHRIS R. KILLMORE, and ELENA V. PERELOMA

The effect of deformation temperature on microstructure and mechanical properties was investigated for thermomechanically processed NbTi-microalloyed steel with ferrite-pearlite microstructure. With a decrease in the finish deformation temperature at 1348 K to 1098 K (1075 °C to 825 °C) temperature range, the ambient temperature yield stress did not vary significantly, work hardening rate decreased, ultimate tensile strength decreased, and elongation to failure increased. These variations in mechanical properties were correlated to the variations in microstructural parameters (such as ferrite grain size, solid solution concentrations, precipitate number density and dislocation density). Calculations based on the measured microstructural parameters suggested the grain refinement, solid solution strengthening, precipitation strengthening, and work hardening contributed up to 32 pct, up to 48 pct, up to 25 pct, and less than 3 pct to the yield stress, respectively. With a decrease in the finish deformation temperature, both the grain size strengthening and solid solution strengthening increased, the precipitation strengthening decreased, and the work hardening contribution did not vary significantly.

DOI: 10.1007/s11661-015-2969-2

I. INTRODUCTION

MICROSTRUCTURE and mechanical properties of steel evolve from a combined effect of chemical composition and parameters of thermomechanical processing (TMP). In high-strength low-alloy steels, addition of precipitate-forming elements, such as Ti, Nb, or V, is commonly applied. High-temperature precipitation retards austenite (γ) recrystallization *via* grain boundary pinning,[1,2] which facilitates ferrite (α) grain refinement. Low-temperature precipitation results in precipitation strengthening[3] and may stimulate dislocation generation which enhances work hardening.[4,5] Following TMP, the steel strength usually increases with (1) an increase in *reheating temperature*,[6,7] which can be attributed to particle dissolution, further precipitation during rolling at a finer scale, stronger grain boundary pinning, and grain refinement; (2) an increase in *deformation strain*,[6,8] due to grain refinement, work hardening (dislocation density increase), and strengthening by strain-induced precipitates; (3) a decrease in *finish rolling temperature*,[7,9–11] due to grain refinement, work hardening (especially if deformation is carried out in two-phase $\alpha + \gamma$ region), and transformation strengthening (formation of bainite or acicular ferrite); and (4) an increase in *cooling rate*,[10] due to grain refinement and transformation strengthening. Although these qualitative trends of microstructure property development during TMP are well understood, comparative contributions of each of the strengthening mechanisms (grain refinement, solid solution strengthening, precipitation strengthening, and work hardening) and their variations with steel composition and TMP parameters still require clarification. For example, in a steel containing 0.044C-0.25Mo-0.0554Nb-0.014Ti, the ferrite grain refinement, solid solution strengthening, and work hardening together contributed up to 65 pct to the yield stress, and the precipitation and transformation (presence of bainite) strengthening contributed 35 pct.[12] In another example, in a steel containing 0.064C-0.0625Nb-0.0435Ti the grain refinement, solid solution strengthening and work hardening together contributed up to 96 pct to the yield stress, and only 4 pct was the contribution from precipitation strengthening,[13] which could be explained by a lower microalloying element content compared to that in.[12] However, in a steel containing 0.06C-0.08Nb-0.07Ti the grain refinement, solid solution strengthening and work hardening together contributed 67 pct to the yield stress, and the remaining 33 pct was the contribution from precipitation strengthening,[14] which is more than 8 times higher compared to that reported in,[13] although the microalloying element content increased by only

ANDRII G. KOSTRYZHEV, Research Fellow, is with the Faculty of Engineering and Information Sciences, School of Mechanical, Materials and Mechatronics Engineering, University of Wollongong, Northfields Avenue, Wollongong, NSW 2522, Australia. Contact e-mail: andrii@uow.edu.au OLEXANDRA O. MARENYCH, Honorary Research Fellow, is with the UOW Electron Microscopy Centre, University of Wollongong, Squires Way, Wollongong, NSW 2519, Australia. CHRIS R. KILLMORE, Product Innovation Specialist: Manufacturing, Construction, and Mining, is with the BlueScope Steel Limited, Five Islands Road, Port Kembla, NSW 2505, Australia. ELENA V. PERELOMA, Professor of Physical Metallurgy, Director, is with the Faculty of Engineering and Information Sciences, School of Mechanical, Materials and Mechatronic Engineering, University of Wollongong, and also with the UOW Electron Microscopy Centre, University of Wollongong.

Manuscript submitted February 4, 2015.

Published online: 20 May 2015

0.044 wt pct. Obviously the variations in steel processing should be taken into account.

In the present work, we studied the effect of deformation temperature on microstructure (grain refinement, solid solute concentrations, precipitation, and dislocation density) and mechanical properties (yield stress, tensile strength, and elongation to failure) for the NbTi-microalloyed steel. Microstructural contributions to the yield stress were calculated using well-known relationships and the measured microstructural parameters. A relative effect of strengthening mechanisms (grain refinement, solid solution and precipitation strengthening, and work hardening) on mechanical properties in our steel is discussed. The effect of chemical composition on the role of these mechanisms in strength formation is discussed on the basis of available literature data.

II. MATERIALS AND EXPERIMENTAL TECHNIQUES

A steel containing 0.081C, 1.20Mn, 0.27Si, 0.021Ni, 0.019Cr, 0.1Mo, 0.016Cu, 0.037Al, 0.064Nb, 0.021Ti, 0.003V, 0.001S, 0.012P, and 0.0047N (wt pct) was provided by BlueScope Steel Ltd. 10 × 15 × 20 mm size samples for TMP simulations were cut from a quarter-thickness position of a 230-mm-thick continuously cast slab. The TMP was carried out using a Gleeble 3500 thermomechanical simulator. The three studied schedules are illustrated in Figure 1. The processing involved austenitizing at 1523 K (1250 °C) for 300 seconds, 0.35 strain of roughing deformation at 1373 K (1100 °C) at 5 s^{-1} strain rate, 0.75 strain of finishing deformation at 1348 K, 1248 K, or 1098 K (1075 °C, 975 °C, or 825 °C) at 5 s^{-1} strain rate, cooling to 873 K (600 °C) at a cooling rate of 1 °C s^{-1}, holding at this temperature for 300 seconds to assure formation of ferrite-pearlite microstructure and air cooling to room temperature. Microstructural investigations of the TMP samples were conducted on the samples cut parallel to the compression plane.

Optical microscopy was carried out using a Leica DMRM microscope equipped with Leica Application Suite (LAS) 4.0.0 image processing software. For the determination of average ferrite grain sizes, 800 to 1000 grains were imaged from the mid-thickness position of each TMP sample. Measurements of the average grain size (equivalent circle diameter) were carried out using Leica Grain Expert software.

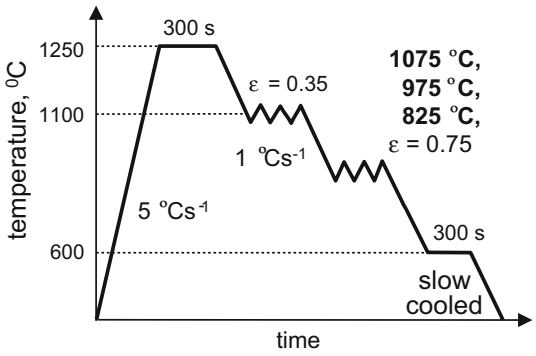

Fig. 1—The schematic diagram of thermomechanical processing.

Scanning electron microscopy of precipitates was carried out using JEOL 7001F FEG scanning electron microscope (SEM) operating at 5 kV. SEM sample preparation included polishing with diamond suspensions and slight etching with 2 pct Nital. For determination of the particle size distributions, number density, and volume fraction values, 150 to 270 particles (depending on TMP condition) were measured. The energy-dispersive X-ray spectroscopy (EDS) semi-quantitative point analysis of precipitates was carried out using an AZtec 2.0 Oxford SEM EDS system. For the determination of NbTi-rich particle compositions, 20 to 25 particles were analyzed for each TMP condition.

Transmission electron microscopy of thin foil and carbon replica samples was carried out using a JEOL JEM2011 transmission electron microscope (TEM) operating at 200 kV. The thin foil specimens were prepared using fine polishing on Leica EM TXP machine and ion milling on Leica EM RES101 and Gatan PIPS machines. For determination of the particle size distributions, number density, and volume fraction values, 140 to 380 particles were imaged for each TMP condition using thin foil samples. The foil thickness was measured utilizing a convergent beam diffraction technique.[15] The average foil thickness was measured to be 95 nm. Precipitate compositions were determined using energy-dispersive X-ray spectroscopy (EDS) point analysis on a JEOL TEM–EDS system. For the particle chemistry determination, 20 to 25 particles were analyzed for each TMP condition using carbon replica samples. For the dislocation density determination, 10 to 15 representative regions were imaged for each TMP condition using two-beam condition technique described elsewhere.[15]

Tensile testing was carried out using an Instron 5566 series 10 kN testing machine and Bluehill 3 operation software. Flat dog-bone type samples of 4-mm gage length, 2-mm width, and 0.8-mm thickness were cut from the Gleeble samples. For each TMP condition, 3 samples were tested at an ambient temperature at a strain rate of 1 × 10^{-3} s^{-1}.

III. RESULTS

A. *Optical Microscopy*

The steel microstructures consisted of ferrite and pearlite for all the TMP conditions (Figure 2). The average ferrite grain size decreased from 16 ± 10 μm at 1348 K (1075 °C) to 13 ± 6 μm at 1248 K (975 °C) and to 11 ± 5 μm at 1098 K (825 °C) temperature of finishing deformation. The second phase (pearlite) content was measured to be 4.3 pct for the 1348 K (1075 °C), 4.2 pct for the 1248 K (975 °C) and 5.3 pct for the 1098 K (825 °C) deformation temperature schedule.

B. *SEM and TEM Study of Precipitates*

SEM revealed the presence of 20 to 170-nm-sized precipitates for all TMP conditions (Figures 3(a)

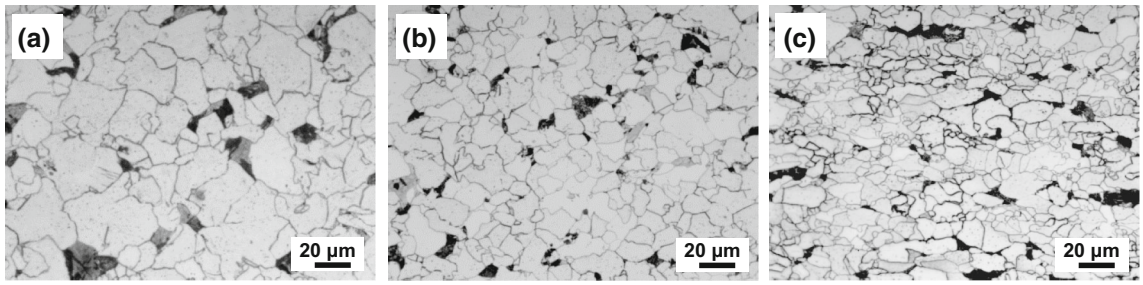

Fig. 2—Representative optical images of ferrite-pearlite microstructures in the studied steel for (*a*) 1348 K (1075 °C), (*b*) 1248 K (975 °C) and (*c*) 1098 K (825 °C) temperatures of finishing deformation.

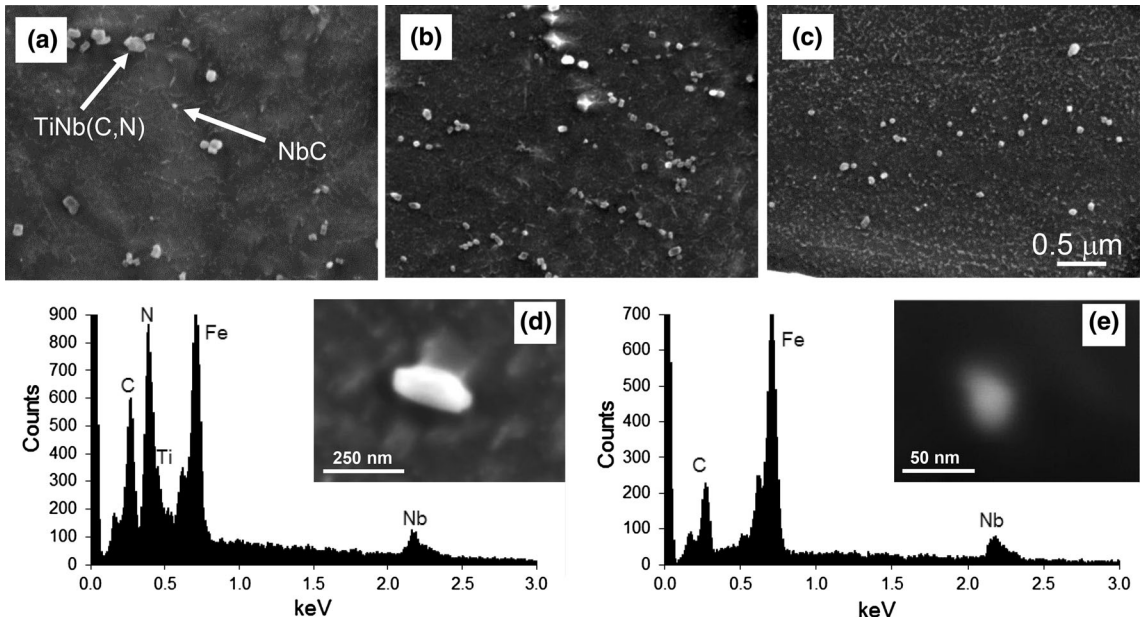

Fig. 3—Representative SEM images of precipitates for (*a*) 1348 K (1075 °C), (*b*) 1248 K (975 °C), and (*c*) 1098 K (825 °C) temperatures of finishing deformation; and EDS spectra of (*d*) TiNb(C,N) and (*e*) NbC particles.

through (c)). SEM–EDS analysis confirmed the particles to be either coarse cuboidal (TiNb)(C,N), coarse ellipsoidal Nb(C,N) or fine spheroidal NbC (Figures 3(d) and (e)). TEM of thin foils revealed the presence of 2 to 20-nm-sized precipitates (Figures 4(a) through (c)) in addition to 20 to 220-nm-sized precipitates detected using carbon replicas (Figures 4(d) through (f)) for all TMP conditions. TEM–EDS analysis has shown the particles to be coarse cuboidal TiNb-rich, coarse ellipsoidal NbTi-rich or fine spheroidal Nb-rich (Figures 4(d) through (f)), which corresponds to the data obtained using SEM–EDS. The particle size, morphology, and chemistry observed in this work correspond to those reported for similar steel compositions and processing parameters.[16–22] The precipitate parameters and compositions varied with TMP schedule (Table I; Figure 5). For particles in the >20 nm size range, the average diameter was the smallest, and the number density and volume fraction were the highest for the 1248 K (975 °C) deformation temperature TMP schedule, compared to other two schedules. For particles in the <20 nm size range, the average diameter did not vary significantly with TMP schedule, the number density was the highest for the 1248 K (975 °C) deformation temperature schedule, and the volume fraction decreased with a decrease in the finish deformation temperature. The amount of Nb-rich particles was found to be maximum for the 1248 K (975 °C) deformation temperature schedule and minimum for the 1098 K (825 °C) deformation temperature schedule.

C. *TEM Study of Dislocation Structure*

Thin foil TEM has shown the presence of irregular dislocation structure for all TMP conditions (Figure 6). Dislocation knots and tangles were occasionally observed in the vicinity of large particles. The average dislocation density in ferrite increased with a decrease in the finish deformation temperature from $4.5 \pm 0.5 \times 10^{13}$ m^{-2} for 1348 K (1075 °C) to $4.6 \pm 0.5 \times 10^{13}$ m^{-2} for 1248 K (975 °C) and to $9.5 \pm 1.1 \times 10^{13}$ m^{-2} for 1098 K (825 °C). The measured values of dislocation density correspond to those reported earlier for ferrite in carbon[23,24] and Nb-microalloyed steels[9,12,19,25] finish

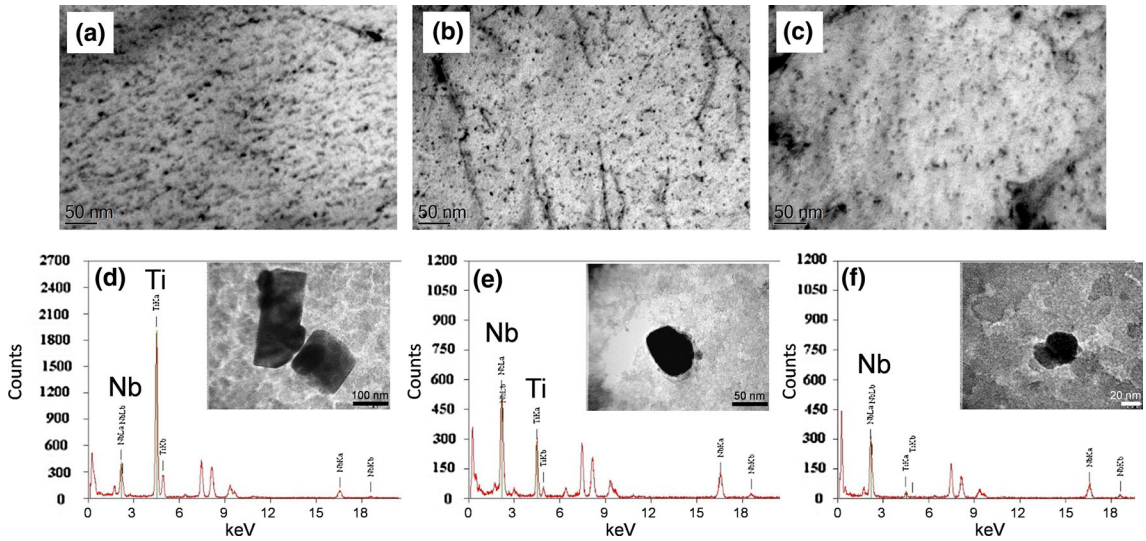

Fig. 4—Representative TEM bright-field images of precipitates for (*a*) 1348 K (1075 °C), (*b*) 1248 K (975 °C), and (*c*) 1098 K (825 °C) temperatures of finishing deformation (thin foil samples); and EDS spectra of (*d*) cuboidal TiNb-rich, (*e*) ellipsoidal NbTi-rich, and (*f*) Nb-rich particles (carbon replica samples).

Table I. Variation in the Particle Parameters with TMP Schedule

Deform. Temp. (K (°C)]	Particle Size Range (nm)	Average Diameter (nm)	Number Density	Volume Fraction*	Composition** (pct)		
					TiNb	NbTi	Nb
1348 (1075)	<20	3 ± 0.8	13,157 μm^{-3}	0.00038	26	52	22
	>20	51 ± 28	1.77 μm^{-2}	0.00470			
1248 (975)	<20	3 ± 0.5	22,428 μm^{-3}	0.00034	12	44	44
	>20	44 ± 30	2.54 μm^{-2}	0.00549			
1098 (825)	<20	3 ± 0.8	8612 μm^{-3}	0.00022	42	42	16
	>20	46 ± 30	1.37 μm^{-2}	0.00325			

*The area fraction of particles, measured using SEM imaging, can be assumed equal to the volume fraction of particles for the high number of particles studied in this work.

**TiNb are those particles for which the EDS peak of Ti is higher than that of Nb, NbTi are those particles for which the EDS peak of Nb is higher than that of Ti.

processed in the same temperature range, *i.e.*, above A_{r3} temperature of austenite-to-ferrite transformation; however, they are several times lower than those after finish rolling in the $\alpha + \gamma$ phase field ($2.3 - 4.0 \times 10^{14}$ m^{-2}[26]) and more than 10 times lower than after finish rolling in ferrite (7×10^{14} m^{-2}[9]).

D. *Mechanical Properties*

The tensile testing of the TMP samples at ambient temperature has shown a significant variation in the stress–strain behaviour with the processing schedule (Figure 7(a)). The yield stress did not vary significantly for all the studied TMP schedules (Table II). With a decrease in the finish deformation temperature, the ultimate tensile strength (UTS) decreased and the elongation to failure increased. Contrary to the continuous yielding behaviour observed for the samples deformed at 1348 K and 1248 K (1075 °C and 975 °C), the stress–strain curve for samples deformed at 1098 K (825 °C) exhibited a discontinuous yielding phenomenon. The work hardening rate exponentially decreased with strain for the 1348 K and 1248 K (1075 °C and 975 °C) deformation temperature schedules (Figure 7(b)). However, for the 1098 K (825 °C) deformation temperature schedule, the work hardening rate showed a period of sharp decrease after the yield point and the minimum (at about 0.055 strain), followed by a period of increase (in the 0.055 to 0.065 strain range) and a period of gradual decrease (up to failure). The average work hardening rate decreased with a decrease in the finish deformation temperature. The ferrite microhardness was measured to be 197 ± 14, 186 ± 13, and 174 ± 7 HV for the 1348 K (1075 °C), 1248 K (975 °C), and 1098 K (825 °C) temperature schedules, respectively. The observed variations in the mechanical properties with TMP followed the variations in microstructure discussed below.

IV. DISCUSSION

A. *Effect of TMP on Microstructure*

The decrease in the ferrite grain size with a decrease in finish deformation temperature observed in the current

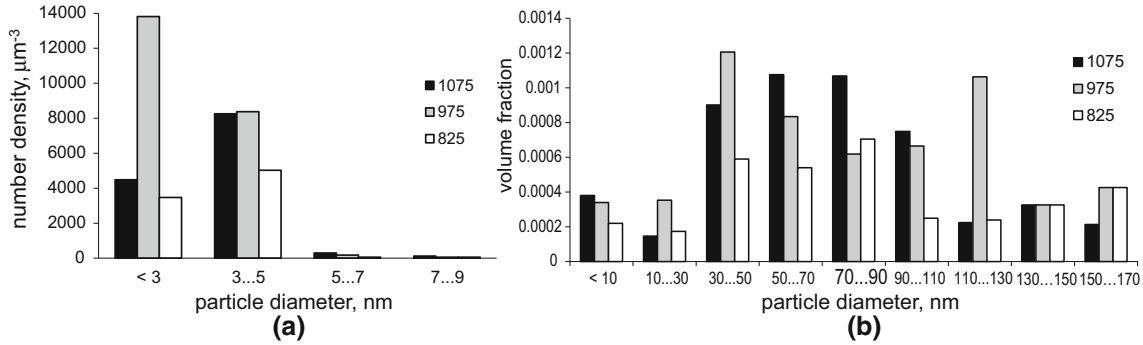

Fig. 5—Precipitate (*a*) size distribution in the <10 nm size range observed by TEM, and (*b*) volume fraction distribution in full size range observed by both TEM and SEM.

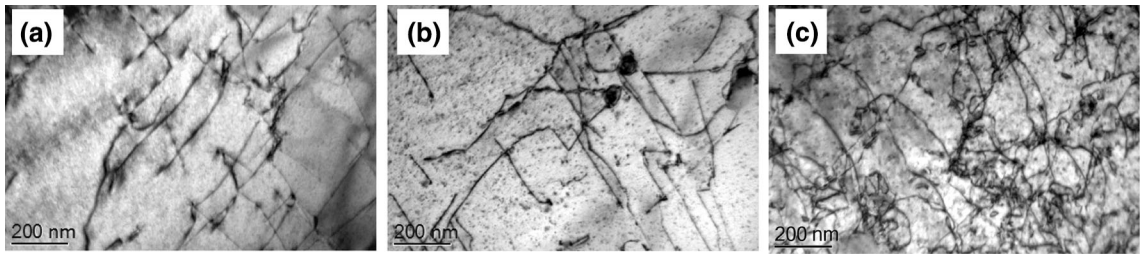

Fig. 6—Representative TEM bright-field images (two-beam condition near [001] zone axis) of dislocation structure for (*a*) 1348 K (1075 °C), (*b*) 1248 K (975 °C), and (*c*) 1098 K (825 °C) temperatures of finishing deformation.

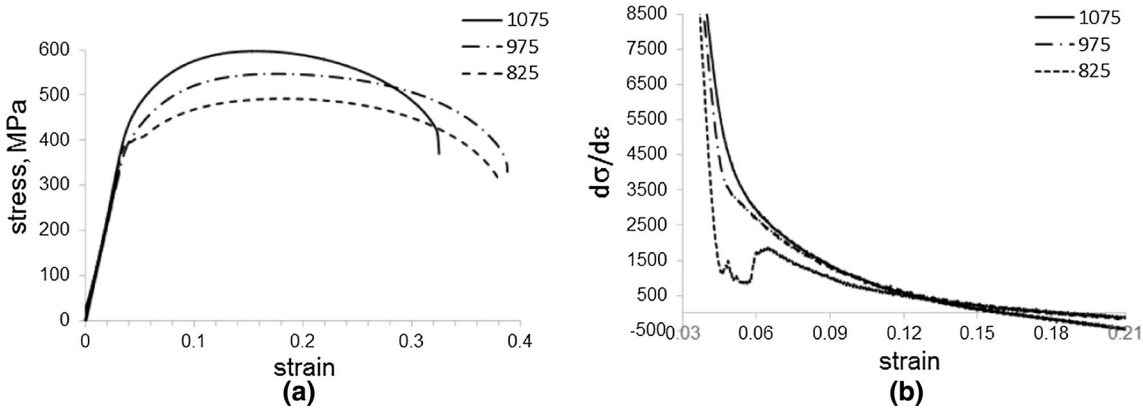

Fig. 7—(*a*) Ambient temperature tensile stress–strain curves and (*b*) work hardening rate variation with strain for three TMP conditions of the studied steel.

Table II. Variation in the Ambient Temperature Mechanical Properties with TMP Schedule

Deform. Temp. [K (°C)]	YS (MPa)	UTS (MPa)	El (pct)
1348 (1075)	405 ± 5	603 ± 5	27 ± 2
1248 (975)	386 ± 9	548 ± 5	32 ± 3
1098 (825)	404 ± 10	498 ± 9	34 ± 2

study is consistent with the austenite grain structure development in the studied steel presented by us in an earlier work.[27] After deformation at 1348 K (1075 °C), the austenite grain structure was fully recrystallized, deformation at 1248 K (975 °C) resulted in partial recrystallization, and deformation at 1098 K (825 °C) led to the formation of pan-caked microstructure with elongated non-recrystallized austenitic grains. A larger amount of crystal defects (shear bands, sub-grain boundaries, and dislocations) inherent in lower temperature austenitic microstructures resulted in (1) an increased number of the ferrite nucleation sites during phase transformation and (2) the ferrite grain refinement. The grain structure variation with deformation

temperature observed here corresponds to the well-documented dependences studied earlier.[28]

No significant variation with TMP schedule was observed for the second phase (pearlite) content, which can be attributed to the similarity in cooling rates in the temperature range of austenite-to-ferrite transformation (between A_{r3} and A_{r1}). However, the measured amount of second phase (4.2 to 5.3 pct) is almost 2 times lower than the value which might be expected (8 pct) from the lever rule for the carbon content in the studied steel composition. This can be explained by consumption of carbon by carbonitride precipitation in austenite, *i.e.*, prior to the austenite-to-pearlite transformation.

Parameters of NbTi-rich precipitates significantly varied with TMP schedule (Table I; Figure 5), which reflects a variation in precipitation kinetics with deformation temperature. The particle number density in both studied size ranges (<20 and >20 nm), volume fraction in the >20 nm size range, and a relative amount of pure Nb-rich particles (to the total amount analyzed) all showed a maximum value for the 1248 K (975 °C) deformation temperature schedule. These indicate a strong driving force for precipitation during and after deformation at 1248 K (975 °C) and support the expectation for high rate of strain-induced precipitation at this temperature. According to the earlier studies,[1,29,30] the nose of Nb(C,N) time–temperature–precipitation diagram falls in the temperature range of 1173 K to 1373 K (900 °C to 1000 °C), although a particular temperature value of maximum precipitation rate (minimum precipitation start time) may vary with the steel composition and processing parameters. The particle number density and volume fraction in both studied size ranges (<20 and >20 nm) and a relative amount of Nb-rich particles (to the total amount analyzed) showed a minimum value for the 1098 K (825 °C) deformation temperature schedule. These correspond to a decrease in ferrite precipitation with a decrease in austenite deformation temperature reported by us earlier.[31]

The dislocation density in ferrite did increase with a decrease in the finish deformation temperature, due to retardation of dislocation annihilation with a decrease in temperature. However, the dislocation density variation from the 1348 K (1075 °C) deformation temperature schedule to the 1248 K (975 °C) deformation temperature schedule was insignificant (about 2 pct), although the variation to the 1098 K (825 °C) deformation temperature schedule was more than 2 times. This can be related to the 1098 K (825 °C) temperature being significantly below the non-recrystallization temperature of the studied steel, $T_{nr} \sim 1248$ K (975 °C),[32] which resulted in significant strain hardening of austenite and retardation of dislocation annihilation leading to the noticeable increase in the final dislocation density in ferrite.

B. *Effect of TMP on Mechanical Properties*

The stress–strain behavior of the studied steel during tensile testing at ambient temperature varied with the processing schedule (Figure 7). With a decrease in the finish deformation temperature, both stress–strain curve and work hardening rate dependence on strain shifted downward, *i.e.*, to lower stress and work hardening rate values. For example, at 0.055 strain, the work hardening rate decreased from 3400 for the 1348 K (1075 °C) to 3000 for the 1248 K (975 °C) and to 840 for the 1098 K (825 °C) finish deformation temperature schedule. In contrast to the exponential decrease in work hardening rate with strain observed for the 1348 K (1075 °C) and 1248 K (975 °C) deformation temperature schedules, the work hardening rate for the 1098 K (825 °C) deformation temperature schedule showed a minimum shortly after the yield point. These can be related to the variation in the particle number density and dislocation density with the finish deformation temperature and the subsequent effect of these parameters on work hardening behavior during testing. In this work with a decrease in the finish deformation temperature, the particle number density decreased, which resulted in a decrease in potential number of dislocation–particle interaction sites, and the total dislocation density increased, which could result in an increase in the density of mobile dislocations, lower dislocation generation rate, and lower work hardening rate for a lower finish deformation temperature schedule. A decrease in work hardening rate with a decrease in precipitate number density has been shown previously for Nb-microalloyed line pipe steels.[33] A decrease in work hardening rate with an increase in the dislocation density in ferrite was observed previously in bake-hardened TRIP and DP steels.[34] The discontinuous yielding behavior observed here for the samples deformed at 1098 K (825 °C) could be related to the formation of Cottrell atmospheres. However, the carbon content in solid solution was similar for all the studied TMP conditions (see the calculations below). Therefore, the formation of Cottrell atmospheres should not be considered as the primary reason for the discontinuous yielding observed here. This behavior can be related to an increased Nb content in solution for the samples deformed at 1098 K (825 °C) (see the calculations below), although Nb is a substitutional element. Recently published data showed the additions of Ni (another substitutional element) leading to appearance of discontinuous yielding in a ferritic steel.[35] This phenomenon was explained by the grain boundary strengthening due to Ni segregation to the boundaries followed by an enhanced dislocation generation from the boundaries during loading. Nature of this phenomenon with respect to Nb in solution requires further investigation.

The yield stress did not vary significantly for all the studied TMP conditions (Table II), although the average ferrite grain size decreased with a decrease in deformation temperature. This can be explained by the effect of precipitation: the particle number density and volume fraction decreased with a decrease in deformation temperature (Table I; Figure 5), which resulted in the decrease in precipitation strengthening effect and compensated a possible yield stress increase due to grain refinement.

The UTS gradually decreased with a decrease in the finish deformation temperature (Table II), which corresponds to some earlier published results[7,36], although other studies[6,9,10,37] showed an increase in UTS with a

decrease in the finish deformation temperature. This discrepancy in UTS behavior can be related to the variation in temperature range which was applied during finish rolling. When hot rolling was carried out below the austenite-to-ferrite transformation temperature A_{r3}, a decrease in the finish deformation temperature resulted in the UTS increase,[6,9,10,37] due to an increase in work hardening (formation of deformation bands and dislocation pile-ups) with a decrease in temperature. However, when hot rolling was completed above A_{r3} temperature, similar to this work, the UTS decreased with a decrease in the finish deformation temperature.[7,36] A decrease in UTS with a decrease in the finish deformation temperature follows a decrease in the work hardening rate and a decrease in the precipitate number density as discussed above. A decrease in UTS with a decrease in the precipitate number density has been shown previously for the Nb-microalloyed line pipe steels[33] and TRIP steels.[38]

The elongation to failure (ductility) increased with a decrease in the finish deformation temperature (Table II) inversely following the decrease in work hardening rate and UTS (strength).

C. *Effect of Strengthening Mechanisms on the Yield Stress*

To assess the relative effect of various strengthening mechanisms on the yield stress, their contributions have been calculated as shown below.

The grain refinement contribution was estimated using the Hall–Petch equation:

$$\sigma_{gs} = \sigma_0 + k \cdot d^{-1/2}, \qquad [1]$$

where $\sigma_0 = 15$ MPa and $k = 21.4$ MPa mm$^{1/2}$ for pure iron[39] were accepted in this work to evaluate only the influence of ferrite grain size, d.

As expected, the grain refinement contribution to the yield stress increased with a decrease in the finish deformation temperature (Table III) due to a decrease in the average ferrite grain size.

A possible increment to the yield stress from pearlite was neglected due to the low measured amount of this phase (4.2 to 5.3 pct).

The solid solution strengthening from Mn, Si, C, and Nb was estimated using the matrix concentrations of these elements and the following relationship:[3]

$$\Delta\sigma_{ss} = 83 \cdot C_{Si} + 32 \cdot C_{Mn} + 5544 \cdot C_C + 4230 \cdot C_{Nb}, \qquad [2]$$

where C_{Si}, C_{Mn}, C_C, and C_{Nb} are Si, Mn, C, and Nb concentrations (wt pct) in the ferrite matrix, respectively; 4230 MPa/wt pct of Nb strengthening coefficient was derived from.[40]

The matrix concentrations of Mn and Si were measured with SEM–EDS, and were found to be the same for all three TMP schedules and equal to the contents of these elements in steel composition, *i.e.*, 1.20 wt pct for Mn and 0.27 wt pct for Si. The matrix concentration of Nb was calculated *via* subtraction of the Nb concentration in particles from that in the steel composition. The matrix concentration of C was calculated *via* subtraction of the C contents in pearlite and particles from that in the steel composition.

Considering the carbon content in pearlite phase being equal to the eutectoid carbon concentration, the amount of carbon in pearlite in the studied steel will be

$$\text{C content in pearlite(wt pct)} = \text{measured pearlite fraction} \cdot 0.71,$$

where 0.71 wt pct is the eutectoid carbon concentration assumed on the basis of[41] for 1.2 wt pct of Mn in the studied steel;

$$\text{C content in particles and solution(wt pct)} = 0.081 - \text{C content in pearlite(wt pct)}.$$

For the measured pearlite fractions, the C content in particles and solution together was calculated to be 0.050, 0.051, and 0.043 wt pct for 1348 K, 1248 K, and 1098 K (1075 °C, 975 °C, and 825 °C) temperature schedules, respectively.

For the 20 to 170-nm particles, which were mainly TiNb-rich, the Ti/Nb atomic ratio was assumed to be 3/1.[42] Due to the nitrogen content being relatively low in the steel composition, the N/C atomic ratio in these

Table III. Microstructural Contributions to the Yield Stress

Deform. Temp. [K (°C)]	Calculated Contributions						Tensile YS (MPa)	YS From HV (MPa)		Min. Error (pct)
	Grain Size	Solid Solutes	Precipitates >20 nm	Precipitates <20 nm	Disloc	Total YS		[48]	[49]	
1348 (1075)										
MPa	184	265	64	90	12	615	405	499	493	+23
Percentage	30	43	10	15	2	100				
1248 (975)										
MPa	202	260	78	85	13	638	386	477	465	+34
Percentage	32	41	12	13	2	100				
1098 (825)										
MPa	219	334	57	68	18	696	404	453	435	+54
Percentage	31	48	8	10	3	100				

particles was assumed to be 2/2. For such $Ti_3Nb_1C_2N_2$ precipitates with fcc crystal structure,[42] the >20 nm particle volume fraction can be related to the Nb atomic fraction in these particles in the following way

$$V_{f>20\,\mathrm{nm}} = \frac{4 \cdot N_{\mathrm{Nb}>20\,\mathrm{nm}} \cdot a^3_{\mathrm{Ti_3Nb_1C_2N_2}}}{4} \cdot \frac{2}{N_{\mathrm{Fe}} \cdot a^3_{\mathrm{bccFe}}},$$

$$\mathrm{Nb}_{\mathrm{at}>20\,\mathrm{nm}} = \frac{N_{\mathrm{Nb}>20\,\mathrm{nm}}}{N_{\mathrm{Fe}}},$$

$$\mathrm{Nb}_{\mathrm{at}>20\mathrm{nm}} = \mathrm{V}_{\mathrm{f}>20\mathrm{nm}} \cdot \frac{\mathrm{a}^3_{\mathrm{bccFe}}}{\mathrm{a}^3_{\mathrm{Ti_3Nb_1C_2N_2}} \cdot 2},$$

and to the C atomic fraction in these particles in the following way

$$\mathrm{V}_{\mathrm{f}>20\,\mathrm{nm}} = \frac{2 \cdot \mathrm{N}_{\mathrm{C}>20\mathrm{nm}} \cdot \mathrm{a}^3_{\mathrm{Ti_3Nb_1C_2N_2}}}{4} \cdot \frac{2}{\mathrm{N}_{\mathrm{Fe}} \cdot \mathrm{a}^3_{\mathrm{bccFe}}},$$

$$\mathrm{C}_{\mathrm{at}>20\mathrm{nm}} = V_{f>20\mathrm{nm}} \cdot \frac{\mathrm{a}^3_{\mathrm{bccFe}}}{\mathrm{a}^3_{\mathrm{Ti_3Nb_1C_2N2}}},$$

where $V_{f>20\mathrm{nm}}$ is the >20 nm particle volume fraction, N_{Nb} and N_C are the numbers of Nb and C atoms in >20 nm particles, N_{Fe} is the number of Fe atoms in the studied sample volume, $a_{Ti3Nb1C2N2}$ and a_{bccFe} are the unit cell sizes of $Ti_3Nb_1C_2N_2$ particles and bcc Fe, respectively.

Assuming stoichiometric 50/50 pct concentration of Nb and C atoms in the <20 nm NbC particles with fcc crystal structure,[43–45] the <20 nm particle volume fraction can be related to the Nb and C atomic fractions in these particles in the following way:

$$V_{f<20\mathrm{nm}} = \frac{N_{\mathrm{C}<20\mathrm{nm}} \cdot a^3_{\mathrm{NbC}}}{4} \cdot \frac{2}{N_{\mathrm{Fe}} \cdot a^3_{\mathrm{bccFe}}},$$

$$\mathrm{C}_{\mathrm{at}<20\mathrm{nm}} = \mathrm{Nb}_{\mathrm{at}<20\mathrm{nm}} = V_{f<20\mathrm{nm}} \cdot \frac{2 \cdot a^3_{\mathrm{bccFe}}}{a^3_{\mathrm{NbC}}},$$

where $V_{f<20\mathrm{nm}}$ is the volume fraction of the <20 nm particles and a_{NbC} is the unit cell size of NbC particle.

For the measured particle volume fractions (Table I) and the unit cell sizes $a_{Ti3Nb1C2N2}$ = 0.64 nm (on average from[42]), a_{NbC} = 0.44 nm,[43–45] and a_{bccFe} = 0.286 nm, the C contents in all particles were calculated to be 0.063 at. pct (0.014 wt pct), 0.068 at. pct (0.015 wt pct), and 0.041 at. pct (0.009 wt pct) for the 1348 K, 1248 K, and 1098 K (1075 °C, 975 °C, and 825 °C) temperature schedules, respectively. These gave the C contents in solution being 0.036, 0.036, and 0.034 wt pct for the 1348 K, 1248 K, and 1098 K (1075 °C, 975 °C, and 825 °C) temperature schedules, respectively. The Nb contents in all particles were calculated to be 0.037 at. pct (0.063 wt pct), 0.038 at. pct (0.064 wt pct), and 0.026 at. pct (0.044 wt pct) for the 1348 K, 1248 K, and 1098 K (1075 °C, 975 °C, and 825 °C) temperature schedules, respectively. These gave the Nb contents in solution being 0.001, 0.000, and 0.020 wt pct for the 1348 K, 1248 K, and 1098 K (1075 °C, 975 °C, and 825 °C) temperature schedules, respectively.

Calculation with Eq. [2] showed the highest solid solution strengthening contribution for the 1098 K (825 °C) temperature schedule (Table III), which corresponded to the maximum Nb content in solid solution.

Precipitation strengthening from the 20 to 170 nm particles was estimated using the particle parameters measured with SEM (Table I) and the Ashby–Orowan equation,[3] which assumes the dislocation looping between relatively large particles:

$$\Delta\sigma_{ps1} = \frac{10.8\sqrt{f}}{D} \ln\left(\frac{D}{6.125 \times 10^{-4}}\right), \qquad [3]$$

where f is the particle volume fraction and D is the particle diameter in μm.

Precipitation strengthening from the 2 to 20 nm particles was estimated using the particle parameters measured with TEM (Table I) and the order strengthening relationship,[46] which assumes the dislocation cutting of relatively small coherent particles observed in this steel previously:[31]

$$\Delta\sigma_{ps2} = 0.81 \cdot M \cdot \frac{\gamma}{2b} \cdot \left(\frac{3\pi f}{8}\right)^{0.5}, \qquad [4]$$

where $M = 3$ is the matrix orientation factor, $b = 0.286$ nm is Burgers vector, γ is the matrix–particle interface energy assumed for the Fe-NbC interface to be $\gamma = 1$ Jm^{-2},[44] and f is the particle volume fraction.

The variation in precipitation strengthening (Table III) followed the trend for particle volume fraction in the corresponding particle size ranges (Table I): for >20 nm particles, the maximum precipitation strengthening contribution was observed for the 1248 K (975 °C) temperature schedule; and for <20 nm particles, the contribution decreased with a decrease in the finish deformation temperature.

The work hardening contribution to the yield stress was estimated using the long-range work hardening theory:[47]

$$\Delta\sigma_{wh} = \frac{\alpha}{2\pi} Gb\sqrt{\rho}, \qquad [5]$$

where $\alpha = 0.5$ is a constant, $G = 85{,}000$ MPa is the shear modulus, $b = 0.286$ nm is the Burgers vector, and ρ is the dislocation density.

The work hardening contribution increased with a decrease in the finish deformation temperature (Table III) following an increase in the dislocation density.

Total yield stress was calculated as a summary of the microstructural contributions:

$$\sigma = \sigma_{gs} + \Delta\sigma_{ss} + \Delta\sigma_{ps1} + \Delta\sigma_{ps2} + \Delta\sigma_{wh}.$$

Total calculated yield stress was compared to the yield stress values measured in this work using sub-sized specimens and to the values calculated using microhardness and the microhardness–yield stress correlation equations YS = 2 × HV + 105[48] and YS = 2.5 × HV[49] (Table III). The yield stress values measured in

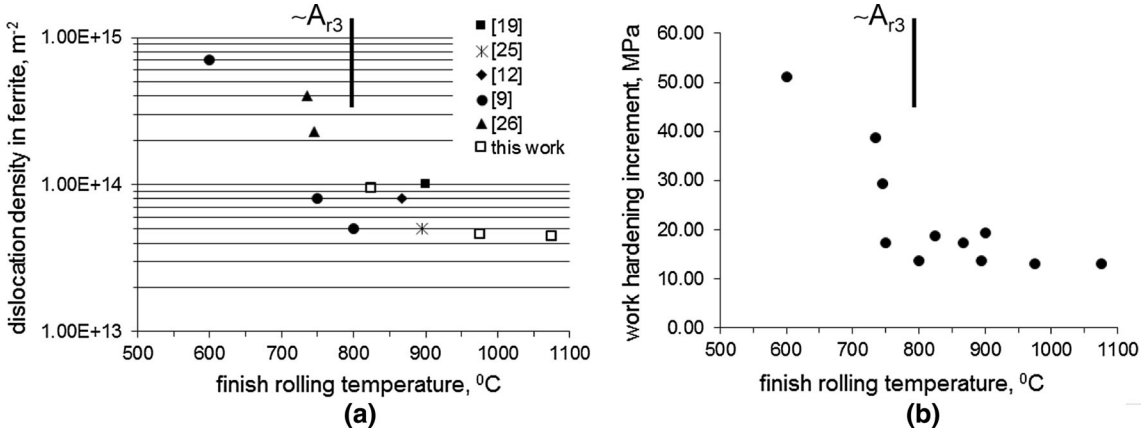

Fig. 8—Effect of the finish deformation temperature on (*a*) dislocation density[9,12,19,25,26] and (*b*) the work hardening contribution to the yield stress estimated using Eq. [5].

this work using tensile testing were lower than those calculated using the microhardness measurements, which can be a result of the specimen size effect on property values. A decrease in measured strength with a decrease in specimen thickness was observed earlier.[50–52] The accuracy of yield stress calculation using the measured microstructural parameters decreased (error increased) with a decrease in deformation temperature. The following reasons can be suggested for this: for the 1348 K (1075 °C) temperature schedule—overestimation of the solid solution strengthening contribution from C solute atoms; for the 1248 K (975 °C) temperature schedule—overestimation of the precipitation strengthening and the solid solution strengthening contribution from C solute atoms; for the 1098 K (825 °C) temperature schedule—overestimation of the solid solution strengthening contributions from C and Nb solute atoms. The applied equations assume that all solute atoms and precipitates become obstacles to the dislocation motion and, therefore, equally contribute to strengthening, although in reality not all the atoms and particles interact with moving dislocations. The amount of non-interacting atoms and particles is likely to increase with an increase in the solid solute concentrations and particle number density. A significant variation between the measured and calculated yield stress values obtained for the 1098 K (825 °C) temperature schedule can be mainly explained by overestimation of the solid solution strengthening contribution from Nb solute atoms: obviously (1) Nb in the form of solid solute atoms contributes to strengthening much weaker than Nb in the form of carbonitride precipitates; and (2) the solid solution strengthening coefficient from Nb atoms, assumed in this work on the basis of[40] being 4230 MPa/wt pct, is overestimated and requires further investigation. In addition, the existing equations for precipitation strengthening and solid solution strengthening disregard dislocation density, although a lower dislocation density, for the same particle distribution and matrix concentrations, should result in a lower strengthening effect, due to a decreased potential number of dislocation–obstacle interaction sites.

The comparative analysis of the calculated microstructural contributions to the yield stress has shown the grain refinement, solid solution, and precipitation strengthening to be responsible for up to 32 pct, up to 48 pct, and up to 25 pct of total strengthening, respectively. The precipitation strengthening from "large" particles (20 to 170 nm size range) was almost equal to that from "small" particles (2 to 20 nm size range). With a decrease in the finish deformation temperature, the grain size strengthening increased and the precipitation strengthening decreased. The work hardening was insignificant (2 to 3 pct), due to the low absolute values of dislocation density resulting from the utilized TMP schedules.

A decrease in the finish deformation temperature below A_{r3} (into the $\alpha + \gamma$ phase field) may result in more than 10 times increase in dislocation density,[9,26] compared to the values observed here for processing above A_{r3} (Figure 8(a)). This may lead to >50 MPa of the work hardening contribution to the yield stress (Figure 8(b)), which would account for about 10 pct of the total strengthening effect (Table IV). With an increase in the cooling rate up to 40 °C s^{-1}, a further increase in dislocation density may lead to >100 MPa of the work hardening contribution[55] (about 20 pct of the yield stress, Table IV), and the bainite formation may additionally give up to 300 MPa[12] (about 50 pct of the yield stress). For the data analyzed here, the joint contribution to the yield stress from grain refinement and solid solution strengthening slightly decreased with an increase in the Nb and Ti contents in steel composition (Figure 9(a)). The precipitation strengthening contribution varied significantly with microalloying: each 0.1 wt pct of Nb + Ti may result in addition of about 100 MPa to the yield stress (Figure 9(a)). However, at about 0.2 wt pct of total Nb + Ti content, the relative effect of precipitation strengthening seems saturating at about 35 pct contribution to the yield stress (Figure 9(b)). This phenomenon requires further investigation.

Table IV. Relative Effect of Microstructural Parameters on Strengthening in Microalloyed Steels

Steel Composition (wt pct)	TMP	Strengthening Contributions (MPa/pct)			YS (MPa)	Derived From Ref.
		Ferrite Grain Size and Solid Solution	Dislocations in Ferrite	Particles		
0.097C-0.017Nb-0.010Ti	FT* = 940	305/84	33/9	25/7	363	[53]
0.10C-0.034Nb	FT = 740	463/90	21/4	31/6	515	[54]
0.04C-0.064Nb	FT = 800	458/76	103/17	42/7	603	[9]
0.064C-0.063Nb-0.043Ti	FT = 900	368/72	123/24	20/4	511	[13]
0.07C-0.086Nb-0.047Ti	FT = 925 CR = 40	405/60	135/20	135/20	675	[55]
0.11C-0.04Nb-0.11Ti	FT = 895 CR# = 10	392/65	66/11	145/24	603	[25]
0.06C-0.08Nb-0.07Ti	FT = 900	325/58	50/9	185/33	560	[14]
0.08C-<0.09Nb-<0.09Ti- <0.09V	FT = 900	322/46	140/20	238/34	700	[56]

FT finish rolling/forging temperature (°C), *CR* cooling rate (°C s^{-1}).

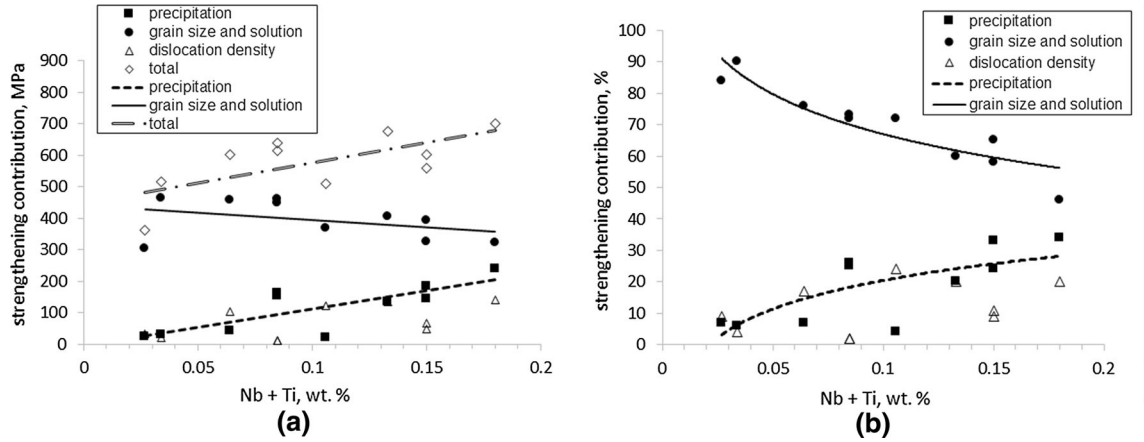

Fig. 9—Effect of Nb + Ti contents in steel composition on (*a*) absolute and (*b*) relative contributions of strengthening mechanisms to the yield stress (based on Tables III and IV).

V. CONCLUSIONS

Investigation of the effect of finish deformation temperature on the microstructure and mechanical properties of an NbTi-microalloyed steel revealed the following:

1. With a decrease in the austenite deformation temperature, the ferrite grain size decreased and the dislocation density in ferrite increased, which is consistent with the earlier published data.
2. The highest NbTi-rich particle number density and volume fraction in ferrite was observed for the 1248 K (975 °C) finish deformation temperature schedule, compared to that of the other two schedules with finish deformation above and below this temperature. This can be a consequence of the 1248 K (975 °C) finish deformation temperature being in the temperature range of minimum precipitation start time for NbC (close to the nose of the time–temperature–precipitation diagram).
3. For finish processing in the 1348 K to 1098 K (1075 °C to 825 °C) temperature range, the ambient temperature yield stress did not show a significant variation with TMP schedule, due to compensation of the increased grain size strengthening by the reduced precipitation strengthening. With a decrease in the austenite deformation temperature, the ambient temperature UTS decreased (elongation to failure increased) as a result of a decrease in the work hardening rate. The ambient temperature work hardening rate decreased with a decrease in the austenite deformation temperature following a decrease in the particle number density (a decrease in the potential number of dislocation–particle interaction sites).
4. For finish deformation above A_{r3} temperature, the calculated contributions to the yield stress from grain refinement, solid solution strengthening, precipitation strengthening, and work hardening were up to 32 pct, up to 48 pct, up to 25 pct, and less than 3 pct, respectively. However, the disagreement between the measured and calculated values of the yield stress could reach 54 pct, due to overestimation of the solid solution strengthening and precipitation strengthening contributions. The work hardening contribution to the yield stress can be expected to increase with a decrease in finish deformation temperature below A_{r3} and with an increase in cooling rate.

5. The literature analysis showed that with an increase in the Nb + Ti content in steel composition, the relative effect of precipitation strengthening on the yield stress increases; however, this effect seems saturating at about 35 pct contribution to the yield stress when the content of these elements exceeds 0.2 wt pct.

ACKNOWLEDGMENTS

The authors are grateful to the Australian Research Council and BlueScope Steel for financial support of the project (LP110100231). Scanning and transmission electron microscopy were carried out using JEOL JSM-7001F FEGSEM (LE0882813) and JEOL JEM-2011 TEM (LE0237478) microscopes at the Electron Microscopy Centre at the University of Wollongong.

REFERENCES

1. B. Dutta and C.M. Sellars: *Mater. Sci. Technol.*, 1987, vol. 3, pp. 197–206.
2. O. Kwon and A.J. DeArdo: *Acta Metall. Mater.*, 1991, vol. 39 (4), pp. 529–38.
3. T. Gladman: *The Physical Metallurgy of Microalloyed Steels*, The Institute of Materials, Cambridge University Press, Cambridge, 1997.
4. R.W. Cahn: *Physical Metallurgy*, North-Holland Publishing, Amsterdam, 1970.
5. F.C. Frank and W.T. Read: *Phys. Rev. Lett.*, 1950, vol. 79, pp. 722–23.
6. S.N. Prasad and D.S. Sarma: *Mater. Sci. Eng. A*, 2005, vol. 408, pp. 53–63.
7. J.K. Patel and B. Wilshire: *J. Mater. Process. Technol.*, 2002, vol. 120, pp. 316–21.
8. C.P. Reip, S. Shanmugam, and R.D.K. Misra: *Mater. Sci. Eng. A*, 2006, vol. 424, pp. 307–17.
9. J. Irvine and T.N. Baker: *Mater. Sci. Eng.*, 1984, vol. 64, pp. 123–34.
10. A. Bakkaloglu: *Mater. Lett.*, 2002, vol. 56, pp. 200–09.
11. L.-Y. Lan, C.-L. Qiu, D.-W. Zhao, and X.-H. Gao: *J. Iron. Steel Res. Int.*, 2011, vol. 18 (2), pp. 57–63.
12. I. Olivares, M. Alanis, R. Mendoza, B. Campillo, and J.A. Juarez-Islas: *Ironmak. Steelmak.*, 2008, vol. 35 (6), pp. 452–57.
13. R. Wang, C.I. Garcia, M. Hua, K. Cho, H. Zhang, and A.J. DeArdo: *ISIJ Int.*, 2006, vol. 46 (9), pp. 1345–53.
14. R.D.K. Misra, K.K. Tenneti, G.C. Weatherly, and G. Tither: *Metall. Mater. Trans. A*, 2003, vol. 34A, pp. 2341–51.
15. D. Williams and C.B. Carter: *Transmission Electron Microscopy, II—Diffraction*, Plenum Press, New York, NY, 1996, pp. 321–23.
16. E.V. Pereloma and J.D. Boyd: *Mater. Sci. Technol.*, 1996, vol. 12, pp. 808–17.
17. A.J. Craven, K. He, L.A. Garvie, and T.N. Baker: *Acta Mater.*, 2000, vol. 48, pp. 3857–68.
18. E.V. Pereloma, B.R. Crawford, and P.D. Hodgson: *Mater. Sci. Eng. A*, 2001, vol. 299, pp. 27–37.
19. R.D.K. Misra, H. Nathani, J.E. Hartmann, and F. Siciliano: *Mater. Sci. Eng. A*, 2005, vol. 394, pp. 339–52.
20. A.G. Kostryzhev, M. Strangwood, and C.L. Davis: *Mater. Technol.*, 2007, vol. 22 (3), pp. 166–72.
21. H.R. Wang and W. Wang: *J. Mater. Sci.*, 2009, vol. 44, pp. 591–600.
22. M. Gomez, P. Valles, and S.F. Medina: *Mater. Sci. Eng. A*, 2011, vol. 528, pp. 4761–73.
23. F. Yin, T. Hanamura, O. Umezawa, and K. Nagai: *Mater. Sci. Eng. A*, 2003, vol. 354, pp. 31–39.
24. H. Yu, Y. Kang, and H. Dong: *J. Univ. Sci. Technol. B.*, 2006, vol. 13 (5), pp. 406–10.
25. H.-J. Kestenbach, S.S. Campos, and E.V. Morales: *Mater. Sci. Technol.*, 2006, vol. 22 (6), pp. 615–26.
26. A.G. Kostryzhev, M. Strangwood, and C.L. Davis: *Mater. Manuf. Process.*, 2010, vol. 25 (1–3), pp. 41–47.
27. A.G. Kostryzhev, A. Al Shahrani, C. Zhu, S.P. Ringer, and E.V. Pereloma: *Mater. Sci. Eng. A*, 2013, vol. 581, pp. 16–25.
28. D.T. Llewellyn and R.C. Hudd: *Steels: Metallurgy and Application*, Butterworth-Heinemann, Oxford, 1998.
29. B. Dutta, E.J. Palmiere, and C.M. Sellars: *Acta Mater.*, 2001, vol. 49, pp. 785–94.
30. S.G. Hong, K.B. Kang, and C.G. Park: *Scripta Mater.*, 2002, vol. 46, pp. 163–68.
31. E.V. Pereloma, A.G. Kostryzhev, A. AlShahrani, C. Zhu, J.M. Cairney, C.R. Killmore, and S.P. Ringer: *Scripta Mater.*, 2014, vol. 75, pp. 74–77.
32. A. Al Shahrani, T. Schambron, A. Dehghan-Manshadi, J. Williams, and E. Pereloma: *Mater. Sci. Forum*, 2010, vols. 654–656, pp. 298–301.
33. A.G. Kostryzhev, M. Strangwood, and C.L. Davis: *Metall. Mater. Trans. A*, 2010, vol. 42A, pp. 3170–77.
34. I.B. Timokhina, P.D. Hodgson, and E.V. Pereloma: *Metall. Mater. Trans. A*, 2007, vol. 38A, pp. 2442–54.
35. D. Akama, N. Nakada, T. Tsuchiyama, S. Takaki, and A. Hironaka: *Scripta Mater.*, 2014, vol. 82, pp. 13–16.
36. Y.W. Kim, J.H. Kim, S.-G. Hong, and C.S. Lee: *Mater. Sci. Eng. A*, 2014, vol. 605, pp. 244–52.
37. H.G. Hillenbrand, E. Amoris, K.A. Niederhoff, C. Perdrix, A. Streißelberger, and U. Zeislmair: EUROPIPE, GmbH, www.europipe.de, 1995.
38. I.B. Timokhina, M. Enomoto, M.K. Miller, and E.V. Pereloma: *Metall. Mater. Trans. A*, 2012, vol. 43A, pp. 2473–83.
39. D.J. Dingly and D. McLean: *Acta Metall.*, 1967, vol. 15, pp. 885–901.
40. Q. Yu, Z. Wang, X. Liu, and G. Wang: *Mater. Sci. Eng. A*, 2004, vol. 379, pp. 384–90.
41. E.C. Bain and H.W. Paxton: *Alloying Elements in Steel*, American Society for Metals, Metals Park, OH, 1961.
42. G.K. Tirumalasetty, M.A. van Huis, C.M. Fang, Q. Xu, F.D. Tichelaar, D.N. Hanlon, J. Sietsma, and H.W. Zandbergen: *Acta Mater.*, 2011, vol. 59, pp. 7406–15.
43. E. Courtois, T. Epicier, and C. Scott: *Micron*, 2006, vol. 37, pp. 492–502.
44. D.H.R. Fors and G. Wahnström: *Phys. Rev. B*, 2010, vol. 82, paper 195410.
45. E.V. Morales, J. Gallego, and H.-J. Kestenbach: *Phil. Mag. Lett.*, 2003, vol. 83, pp. 79–87.
46. D.N. Seidman, E.A. Marquis, and D.C. Dunand: *Acta Mater.*, 2002, vol. 50, pp. 4021–35.
47. A.S. Argon: in *Mechanical Properties of Single-Phase Crystalline Media: Deformation at Low Temperature*, R.W. Cahn and P. Haasen, eds., Physical Metallurgy, North-Holland Publishing, Amsterdam, 1996.
48. S.H. Hashemi: *Mater. Sci. Eng. A*, 2011, vol. 528, pp. 1648–55.
49. W.K. Kim, H.G. Jung, G.T. Park, S.U. Koh, and K.Y. Kim: *Scripta Mater.*, 2010, vol. 62, pp. 195–98.
50. T.A. Kals and R. Eckestein: *J. Mater. Process. Tech.*, 2000, vol. 103, pp. 95–101.
51. Y.H. Zhao, Y.Z. Guo, Q. Wei, A.M. Dangelewicz, C. Xu, Y.T. Zhu, T.G. Langdon, Y.Z. Zhou, and E.J. Lavernia: *Scripta Mater.*, 2008, vol. 59, pp. 627–30.
52. T.N. Goh and H.M. Shang: *J. Mech. Work. Technol.*, 1982, vol. 7, pp. 23–37.
53. He. Kejian and T.N. Baker: *Mater. Sci. Eng., A*, 1993, vol. 169, pp. 53–65.
54. A.G. Kostryzhev: Ph.D. Thesis, University of Birmingham, 2009, http://etheses.bham.ac.uk/436/.
55. M. Charleux, W.J. Poole, M. Militzer, and A. Deschamps: *Metall. Mater. Trans. A*, 2001, vol. 32A, pp. 1635–47.
56. H.-L. Yi, L.-X. Du, G.-D. Wang, and X.-H. Liu: *J. Iron. Steel Res. Int.*, 2008, vol. 15 (2), pp. 76–80.